Journal of Materials Chemistry A

ROYAL SOCIETY OF CHEMISTRY

PAPER

View Article Online
View Journal | View Issue

Check for updates

Cite this: J. Mater. Chem. A, 2026, 14, 2871

Engineered 3D-printed $Bi_4O_5I_2$@hematite scaffolds for visible light photocatalytic degradation of cresols

Akash Rawat, †[a] Raphael B. de Oliveira,†[bc] Tapas Pal,[d] Kleuton A. L. Lima,[c] Guilherme S. L. Fabris,[c] Raphael M. Tromer,[e] Marcelo L. Pereira Junior,[bf] Adarsh Singh,[g] Ashok Kumar Gupta,*[g] Douglas S. Galvão*[c] and Chandra Sekhar Tiwary*[h]

Catalyst leaching hampers reusability in photocatalysis, posing secondary pollution risks. In the present study, $Bi_4O_5I_2$ is decorated onto an engineered 3D-printed hematite scaffold ($Bi_4O_5I_2$@3DH), integrating additive manufacturing with photocatalysis for efficient cresol degradation in diverse water matrices. The hematite grid, fabricated *via* direct ink writing, exhibited excellent rheological behavior (τ_y = 24 Pa), allowing precise shape retention, while $Bi_4O_5I_2$ was immobilized *via* a simple dip-coating method. The $Bi_4O_5I_2$@3DH composite achieved 99.78% degradation of 20 mg L^{-1} *p*-cresol within 240 min and retained 84.28% efficiency after 10 reuse cycles with negligible leaching. Density functional theory (DFT+U) simulations confirmed *S-scheme* heterojunction formation, facilitating interfacial charge transfer (≈−0.9 e^-) and enhanced photocatalytic activity. The engineered scaffold performed consistently across varied water matrices, with *in vitro* and *in silico* analyses revealing reduced toxicity of degradation products. The current work demonstrates a scalable strategy for coupling additive manufacturing with advanced photocatalysis using earth-abundant minerals for sustainable water treatment.

Received 25th September 2025
Accepted 15th November 2025

DOI: 10.1039/d5ta07867a

rsc.li/materials-a

Published on 18 November 2025. Downloaded by Guangxi University on 1/30/2026 3:08:27 AM.

1. Introduction

The economic expansion of a nation is driven by prompt industrialization and urbanization. However, this progress is often accompanied by environmental challenges,[1–3] such as water pollution caused by the discharge of various toxic chemicals into the surface and subsurface water environments.[4–6] One such class of frequently encountered chemicals is cresol, typically originating from industries including coal gasification, coal conversion,[7] chemical production, medicines, petrochemicals, herbicides, and fungicides.[8] Cresols are highly soluble in water, with solubility ranging from 1.9 to 2.5 g/100 mL at room temperature,[9] and are microbial growth inhibitors.[10] Thus, they persist in wastewater treatment plant effluent and receiving water bodies.[11] These xenobiotic chemicals pose a risk to microbes, and their chronic exposure, even at low concentrations, can have pernicious effects on human eyes, skin, mental well-being, and the respiratory system.[12,13] According to the World Health Organization (WHO), the permissible concentration of *p*-cresol in potable water is 1.0 μg L^{-1}.[14] Furthermore, the Federal Water Pollution Control Act classifies cresols as hazardous substances, and the Clean Water Act Amendments (1977 and 1978) regulate their release.[15] Consequently, various treatment technologies, such as photocatalysis,[16,17] adsorption,[18,19] sonolysis,[20] and biodegradation[21] have been explored to mitigate these toxic pollutants. Among these treatments, photocatalysis has emerged as a promising solution,[22,23] owing to its ability to harness solar energy to mineralize a wide range of aqueous pollutants.[24,25] Nevertheless, despite the several advantages of photocatalysis, its practical application is hindered by post-treatment challenges, including the low recovery yield of catalysts and the risk of secondary pollution from their leaching in conventional slurry-based systems.[26,27] To overcome these challenges, Significant efforts have been made towards

[a]School of Environmental Science and Engineering, Indian Institute of Technology Kharagpur, Kharagpur 721302, India
[b]Materials Science and Nano Engineering Department, Rice University, Houston, TX, 77005, USA
[c]Applied Physics Department and Center for Computational Engineering & Sciences, State University of Campinas, Campinas, São Paulo 13083-970, Brazil. E-mail: galvao@ifi.unicamp.br
[d]School of Nano Science and Technology, Indian Institute of Technology Kharagpur, Kharagpur 721302, India
[e]University of Brasília, Institute of Physics, Federal District, Brasilia 70910900, Brazil
[f]University of Brasília, College of Technology, Department of Electrical Engineering, Federal District, Brasilia 70910900, Brazil
[g]Environmental Engineering Division, Department of Civil Engineering, Indian Institute of Technology Kharagpur, Kharagpur - 721302, India. E-mail: agupta@civil.iitkgp.ac.in
[h]Metallurgical and Materials Engineering, Indian Institute of Technology Kharagpur, Kharagpur - 721302, India. E-mail: chandra.tiwary@metal.iitkgp.ac.in
† Equal contribution.

Published on 18 November 2025. Downloaded by Guangxi University on 1/30/2026 3:08:27 AM.

stabilizing the catalysts onto solid supports, including polymers, clay, glass, calcium alginate, ceramics, activated carbon, and metals.[26–34] Although these catalyst carriers reduced the risk of nanoparticle leaching into the treated water, their inert and non-porous nature likely restricted mass transfer and active site accessibility, limiting overall photocatalytic efficiency. Contrastingly, photoactive and porous supports can offer synergistic interactions with the catalyst, enhancing both mass transport and exposure of active sites to reactants, thus improving photocatalytic performance. In this context, additive manufacturing (AM) is highly suitable and an attractive technique for fabricating engineered catalyst supports.[35] The AM allows the design of structures from basic to complex geometries, offering a higher area-to-volume ratio at the macroscopic level than conventional supports.[36–38] Among various 3D printing methods,[39] direct ink writing (DIW) is typically preferred due to its cost-effectiveness, facile operation, and ability to print a wide range of materials, including metals, ceramics, polymers, and glass.[40–42] Essentially, DIW inks require thixotropic properties to ensure shear-thinning and high viscosity, allowing them to withstand their shape post-extrusion.[42–45] The concentration of particle additives significantly influences the ink's viscosity and shear-thinning behaviour,[46] and these additives are typically removed to generate porous 3D printed structures,[47] where the additive concentration directly governs porosity.[48,49]

Natural hematite has abundant reserves and notable capabilities for visible light absorption.[26,50,51] However, its effectiveness in photocatalysis is constrained by low electron transport efficiency and a tendency for rapid charge carrier (e^-/h^+) recombination.[52] Unlike the inert supports mentioned above, when a semiconductor material such as hematite is decorated with a visible-light-driven photocatalyst such as $Bi_4O_5I_2$, its inherent optical properties can be controlled more effectively.[26] Given this, the present investigation focuses on the decoration of $Bi_4O_5I_2$ onto 3D-printed hematite scaffolds (3DH) through an iterative dipping and drying methodology (referred to as $Bi_4O_5I_2$@3DH). Moreover, to gain further insights into the physical mechanisms of the interaction between $Bi_4O_5I_2$ and the 3DH we also carried out *ab initio* simulations. Initially, the factors affecting Photocatalytic Degradation (PCD), such as the amount of catalyst coated (L), infill density ratio (IDR) of the scaffold, initial pollutant concentration (C_0), and pH values, are optimised through the degradation of model pollutant *p*-cresol. Further, the optimized $Bi_4O_5I_2$@3DH structure was thoroughly characterized to determine the physicochemical and electronic properties that eventually influence the photocatalytic process. Subsequently, the real field applicability of $Bi_4O_5I_2$@3DH was assessed in various water matrices. Furthermore, post-treatment analysis of treated aqueous *p*-cresol, including anticipation of degradation products and their biotoxicity, was evaluated using analytical methods and Quantitative Structure–Activity Relationship (QSAR) techniques.

2. Experimental

2.1. Materials and chemical reagents

All chemical reagents provided in the S1 section of the SI were used without further purification. However, the hematite ore collected from the Department of Mining, IIT Kharagpur, was washed thoroughly using deionized (DI) water.

2.2. Instrumentation and characterization

The instruments used for characterization are listed in Section S2 of the SI.

2.3. Fabrication of $Bi_4O_5I_2$@3DH

The $Bi_4O_5I_2$@3DH was synthesized through a three-stage process involving scaffold fabrication, $Bi_4O_5I_2$ synthesis, and their immobilization, as illustrated in Fig. 1 and detailed below.

2.3.1. 3D printing of hematite scaffold (3DH). The ink was initially prepared by dissolving 5% (g mL^{-1}) carboxymethyl cellulose (CMC) in DI water, wherein CMC served as a binder. Although CMC is inherently hydrophilic due to its carboxymethyl groups, the solution was stirred at 500 rpm on a hot plate at 90 °C to ensure homogeneous dispersion. Finely ground hematite powder was then incorporated into the solution in an appropriate proportion to achieve the desired thixotropic behavior suitable for DIW. The resulting ink was utilized to fabricate hematite grids with varying IDR (25%, 50%, and 75%) using a DIW printer (Hyrel Engine HR, USA). Prior to printing, a digital model was created using the REPETREL (version 42.305) slicing software. After several design iterations, the optimized printing parameters were finalized and are presented in Table S1. These included a slice height of 0.6 mm, a nozzle diameter of 1.2 mm, a printing speed of 1 mm s^{-1}, and a grid infill pattern, with all operations conducted at room temperature (Video S1). The as-printed green hematite structures were air-dried at room temperature for a day, then sintered in a muffle furnace at 950 °C for 6 h with a heating ramp rate of 5 °C min^{-1}. The sintered structures were allowed to cool naturally to room temperature and are referred to as 3D-printed hematite scaffolds (3DHs).

2.3.2. Synthesis of $Bi_4O_5I_2$ photocatalyst. Briefly,[26] 1.66 g of KI was dissolved in 40 mL of EG under constant stirring. Subsequently, 2.425 g of $Bi(NO_3)_3 \cdot 5H_2O$ was introduced to this KI solution, ensuring thorough mixing. Following this, the pH of the resulting mixture was adjusted to 9 using 1 M NaOH, and stirred further for two hours. The final product, $Bi_4O_5I_2$, was washed with DI water and ethanol and dried overnight at 65 °C in a hot air oven.

2.3.3. Fabrication of $Bi_4O_5I_2$@3DH. In a 100 mL beaker, 1% (w/v) coating suspension was prepared by adding 200 mg of $Bi_4O_5I_2$ photocatalyst in 20 mL DI water, followed by ultrasonication for 30 min to attain uniform dispersion. Afterwards, the as-fabricated 3DH was immersed in suspension for 30 seconds and then gradually withdrawn, constituting a dip-coating cycle (N). Three separate 3DH samples were subjected to 5, 10, and 20 dip cycles to optimize photocatalyst loading. Notably, after each cycle, the coated 3DH was dried at 80 °C for 2 h in a hot air oven. However, following the final dip, the $Bi_4O_5I_2$ decorated 3DH composites were dried for a day at 65 °C and are hereafter referred to as $Bi_4O_5I_2$@3DH scaffold. Fig. 2a and b present the $Bi_4O_5I_2$@3DH samples with varied N and IDR values.

 This journal is © The Royal Society of Chemistry 2026

Published on 18 November 2025. Downloaded by Guangxi University on 1/30/2026 3:08:27 AM.

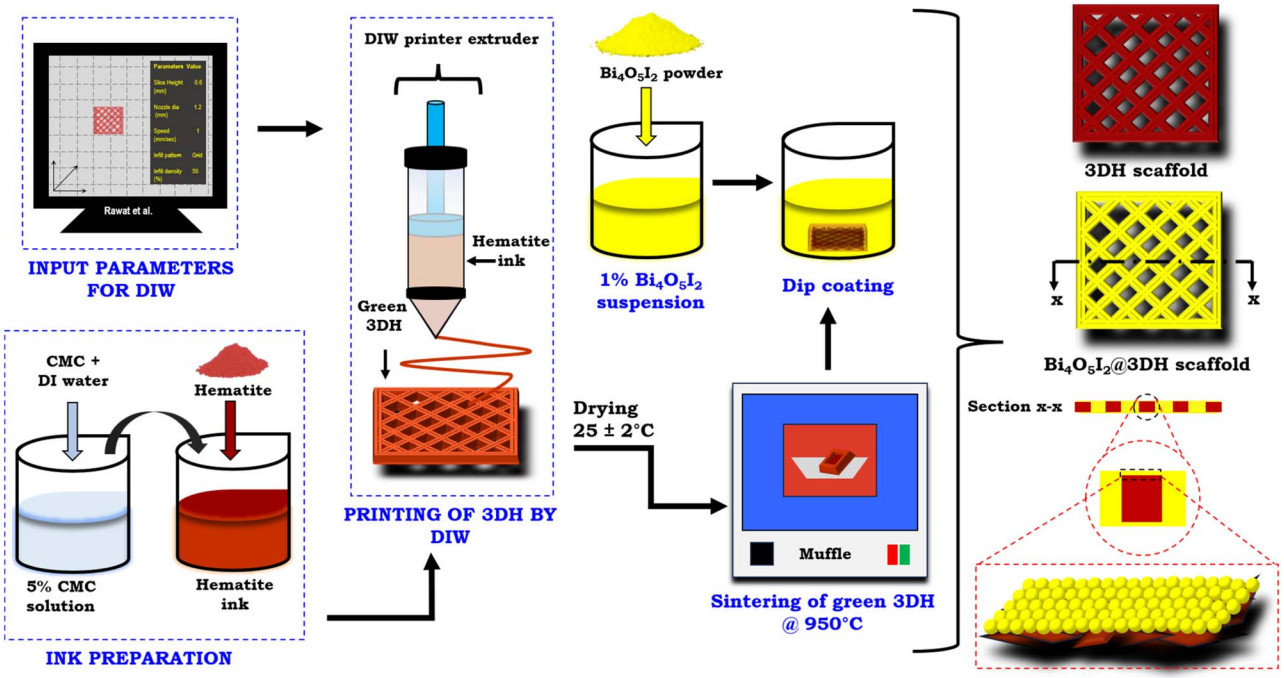

Fig. 1 Fabrication of $Bi_4O_5I_2$ decorated hematite scaffold ($Bi_4O_5I_2$@3DH) using the REPETREL software to define hematite printing parameters for direct ink writing, followed by dip-coating for immobilization of $Bi_4O_5I_2$ nanoparticles onto the sintered hematite grid.

2.4. Experimental set-up and procedure

The photocatalytic reactor (PCR), illustrated in Fig. 2c, primarily comprises a 50 watt LED light source, a 200 mL jacketed beaker, a stainless-steel frame for sample holding, and a magnetic stirrer. Apart from the inclusion of the steel frame, the reactor configuration remains consistent with that employed in our previous studies.[4,26] Further details of the experimental setup with a photograph of PCR are provided in Section S3 and Fig. S1 of the SI, and a real-time video of the PCR during photocatalysis is available as Video S2.

The experimental procedure started with dark adsorption studies to determine the time required to attain adsorption–desorption equilibrium, using 20 mg L^{-1} *p*-cresol solution and fabricated samples. Accordingly, all subsequent photocatalytic experiments adopted the optimized dark phase duration. A one-variable-at-a-time (OVAT) approach was employed to systematically evaluate key operational parameters, starting with the optimization of *N* and IDR values.[4] Followed by investigations into the effects of C_0, solution pH, and cresol derivatives. The residual concentrations of *p*-cresol were quantified using high-performance liquid chromatography (HPLC) or total organic carbon (TOC) analysis. The detailed experimental procedure is provided in Section S4 of the SI.

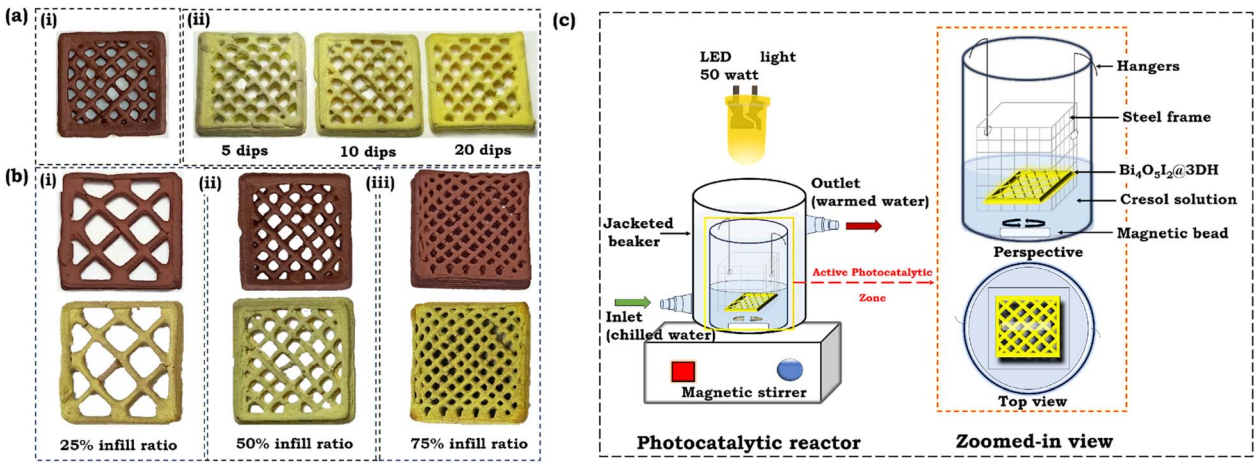

Fig. 2 (a) Variation in the number of dip cycles (*N*) for 3D-printed hematite scaffold (i), decorated with $Bi_4O_5I_2$ (*i.e.*, $Bi_4O_5I_2$@3DH) for (ii) $N = 5$, 10, and 20. (b) Bare hematite and $Bi_4O_5I_2$@3DH ($N = 10$) with varying grid infill density ratios, (i) 25%, (ii) 50%, and (iii) 75%. (c) Experimental set-up endowed with the zoomed-in view, employed for the photocatalysis experiment.

Published on 18 November 2025. Downloaded by Guangxi University on 1/30/2026 3:08:27 AM.

2.5. Density functional theory calculations

The methodology used for the Density Functional Theory (DFT) simulations is provided in Section S5, and the optimized structures illustrating bulk hematite, $Bi_4O_5I_2$, and the hematite (001) surface with the 4 × 4 supercell are depicted in Fig. S2.

2.6. Ecotoxicity evaluation

The colony-forming unit (CFU) method was employed to assess the bio-toxicity of photocatalytically treated water against *E. coli*, as per studies.[4,26,53,54] In addition, *in silico* toxicity prediction was conducted using the Toxicity Estimation Software Tool (T.E.S.T.),[55] which applies QSAR models to estimate the potential toxicity of the intermediates formed during and after the PCD of *p*-cresol.[54]

3. Results and discussion

3.1. Rheological analysis of DIW ink

Fig. S3a shows that shear stress increases with shear rate, while Fig. S3b demonstrates that shear viscosity decreases with shear rate, confirming shear-thinning behavior that allows smooth ink flow through the nozzle under low extrusion pressure during DIW. Shear thinning is a non-Newtonian characteristic, which is desirable for DIW applications.[56] When extrusion pressure is applied to the syringe, the ink flows toward the nozzle tip, where it encounters a high shear rate and reduced viscosity, thus facilitating improved printability. Upon exiting the nozzle, the ink experiences a lower shear rate and higher viscosity, which is crucial for maintaining the dimensional stability of the printed structure.[57,58]

Fig. S3c presents the plot of storage modulus (G') and loss modulus (G'') as a function of shear stress. The values of G' and G″ provide insight into the ink's solid-like and liquid-like behavior, respectively.[59] When $G' > G''$, the ink behaves like an elastic solid, which contributes to shape retention after printing. Conversely, when $G' < G''$, the ink exhibits liquid-like behavior and cannot maintain a defined shape upon deposition. At the point where $G' = G''$, the ink exhibits a gel-like behavior.[37,60] The intersection of the G' and G'' curves indicates the yield stress (τ_y), which marks the transition from solid-like to liquid-like behavior.[61] In the present investigation, the ink demonstrated a yield stress of 24 Pa. The ink shows excellent shape retention at lower shear stress levels, where $G' > G''$ – even when multiple layers are printed. Beyond the yield point, G'' exceeds G' (*i.e.*, $G' < G''$), enabling the ink to flow easily through the nozzle during extrusion.[56,62]

3.2. Characterization of $Bi_4O_5I_2$@3DH

The field emission gun scanning electron microscope (FEG-SEM) images of the 3DH scaffold and $Bi_4O_5I_2$@3DH composite are depicted in Fig. 3a, demonstrating their morphological features. The FEG-SEM image of the bare 3DH scaffold (Fig. 3a(i)) reveals the emergence of macro-porosity, which could be attributed to thermal expansion/contraction during the sintering/cooling processes. The high-magnification image (Fig. 3a(ii)) shows micro and nanopores distributed over the 3DH surface (surrounded by hematite crystals), likely formed due to the decomposition of the CMC binder during sintering at a given temperature.[63] These micropores could act as potential anchoring sites for $Bi_4O_5I_2$ nanoparticles. As evident from Fig. 3a(iii), the $Bi_4O_5I_2$ coating reduces the apparent macro-porosity, while the micropores appear to be filled with $Bi_4O_5I_2$ nanoparticles, as shown in Fig. 3a(iv), reinforcing stronger integration.

The X-ray diffraction (XRD) patterns of $Bi_4O_5I_2$@3DH, $Bi_4O_5I_2$, and 3DH are presented in Fig. 3b. As displayed, the composite sample ($Bi_4O_5I_2$@3DH) exhibits distinct diffraction peaks attributable to both 3DH and $Bi_4O_5I_2$, confirming the successful deposition of $Bi_4O_5I_2$ nanoparticles onto the 3DH scaffold. Specifically, the diffraction peaks at 2θ values of 28.10°, 31.45°, 45.15°, 49.30°, and 54.40° correspond to the (−114), (020), (224), (−424), and (118) planes of $Bi_4O_5I_2$. Whereas peaks located at 33.08°, 35.60°, 49.24°, 54.00°, 62.40°, and 63.90° are assigned to the (012), (104), (110), (024), (116), (214), and (300) planes of hematite.[64,65] The XRD patterns closely match the standard reference cards #96-810-4104 for monoclinic $Bi_4O_5I_2$ (a = 11.26 Å, b = 5.7 Å, c = 14.95 Å)[66,67] and #00-024-0072 for rhombohedral hematite ($a = b = 5.038$ Å, $c = 13.72$ Å).[68] Notably, a slight shift in the diffraction peaks towards lower 2θ values is observed in the composite, indicating possible lattice strain or interfacial interaction between the constituent materials, also noticed by other authors in their investigations.[4,26,69,70] Such structural coupling is anticipated to facilitate improved charge separation and thereby enhance the PCD of cresols.

In addition, our previous study has comprehensively established the optical properties, including ultraviolet-visible diffuse reflectance spectroscopy (UV-DRS), photoluminescence (PL) spectroscopy and ultraviolet photoemission spectroscopy (UPS), and electrochemical behavior such as electrochemical impedance spectroscopy (EIS) of hematite, $Bi_4O_5I_2$ and the hematite/$Bi_4O_5I_2$ composite.

3.3. Photocatalytic performance of the $Bi_4O_5I_2$@3DH scaffold

The synergetic interaction between adsorption and photocatalysis is extensively documented in the literature.[71] In view of this, a one-hour adsorption study was conducted under the given operational parameters (corresponding cresol isomer concentration: 20 mg L^{-1}; IDR: 50%; N: 5; pH: 6.5), shown in Fig. S4a–c. The adsorption of the model contaminant (*p*-cresol) was found to be less than 1% (Fig. S4a). In contrast, saturation in the adsorption of *o*-cresol (Fig. S4b) and *m*-cresol (Fig. S4c) was achieved within 30 min, with adsorption efficiencies reaching approximately 10.3%, which was significant and could not be ignored. Hence, the initial 30 min of the PCD experiments were conducted in the dark to attain the adsorption–desorption equilibrium.

3.3.1. Factors influencing the PCD of *p*-cresols

(i) Number of dip-cycles. Optimizing the value N is critical, as it directly affects the amount of $Bi_4O_5I_2$ catalyst loaded onto the 3DH scaffold, an important parameter influencing photocatalytic activity. As indicated in the inset of Fig. 3c, the 5, 10,

 This journal is © The Royal Society of Chemistry 2026

Published on 18 November 2025. Downloaded by Guangxi University on 1/30/2026 3:08:27 AM.

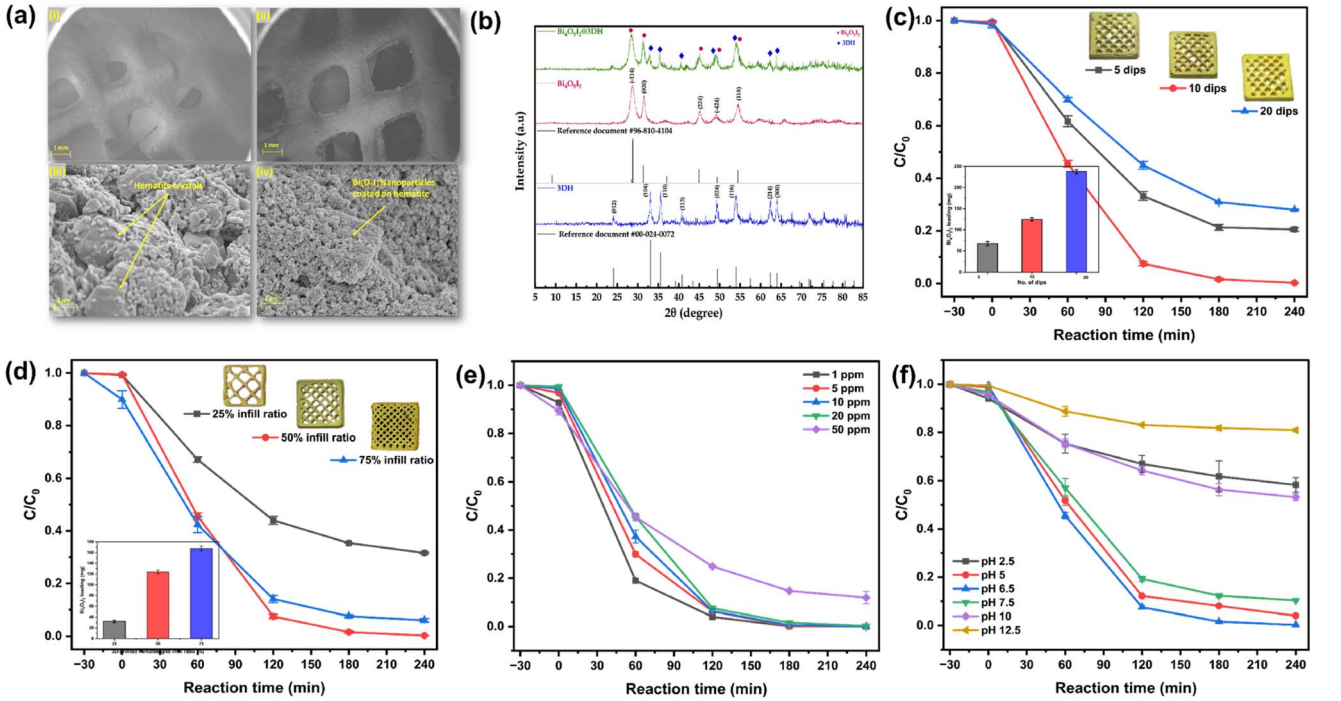

Fig. 3 (a) FEG-SEM images of materials: low magnification SEM images of (i) 3D-printed hematite, *i.e.*, 3DH, and (ii) $Bi_4O_5I_2$-coated 3DH, *i.e.*, $Bi_4O_5I_2$@3DH; high magnification SEM images of (iii) 3DH and (iv) $Bi_4O_5I_2$@3DH. (b) XRD pattern of $Bi_4O_5I_2$@3DH, $Bi_4O_5I_2$, reference document no. 96-810-4104, 3DH, and reference document no. 00-024-0072. Influence of operational parameters on the PCD of model contaminant (*p*-cresol): (c) number of $Bi_4O_5I_2$ solution dips ($N = 5$, 10, and 20) [provided: 50% grid IDR, initial *p*-cresol concentration (C_0) = 20 ppm, and pH = 6.5], (d) IDR of 3DH (=25, 50, and 75%) [provided: $N = 10$, $C_0 = 20$ ppm, and pH = 6.5], (e) C_0 [provided: $N = 10$, IDR = 50%, and pH = 6.5] and (f) initial pH of *p*-cresol solution, [provided: $N = 10$, IDR = 50%, and $C_0 = 20$ mg L^{-1}].

and 20 N values resulted in L values of approximately 67.1 ± 4.7 mg, 124.6 ± 4.2 mg, and 237.6 ± 5.3 mg, respectively. Their corresponding PCD efficiencies against *p*-cresol (20 mg L^{-1}) are illustrated in Fig. 3c, revealing that the composite with $N = 10$ achieved the highest PCD efficiency (99.78%), followed by $N = 5$ (79.52%) and $N = 20$ (71.6%). The lower activity at $N = 5$ is likely a result of insufficient catalyst loading, which limited light absorption necessary for efficient PCD.[72] In contrast, the decreased efficiency at $N = 20$ is attributed to excessive catalyst deposition, possibly leading to agglomeration, blockage of active sites, and the formation of a thick layer that suppressed the active role of the 3DH scaffold.[72,73] The $N = 10$ condition provided an optimal balance, enabling synergistic interaction between $Bi_4O_5I_2$ and the 3DH structure. The abovementioned findings highlight the importance of tuning catalyst loading on semiconductor substrates employed for dual functionalities, including synergistic interaction as an active support and an immobilising carrier, ensuring effective interaction between the photocatalyst and the scaffold.

(ii) Infill density ratio of 3DH scaffold. Fig. 3d displays the influence of the IDR of the 3DH scaffold on the PCD of 20 mg L^{-1} *p*-cresol. Scaffolds with 25%, 50%, and 75% IDR were fabricated, carrying corresponding average weights of 2.751 ± 0.129 g, 2.262 ± 0.264 g, and 5.513 ± 0.059 g. As anticipated and displayed in the inset of Fig. 3d, after the application of $Bi_4O_5I_2$ coating ($N = 10$), the respective measured weights of $Bi_4O_5I_2$@3DH composites increased to 2.783 ± 0.131 g ($L = 32.3 \pm 2.2$ mg), 3.386 ± 0.263 g ($L = 123.6 \pm 3.6$ mg), and 5.680 ± 0.054 g ($L = 167.5 \pm 4.5$ mg). Furthermore, under 4 h of LED irradiation, the observed PCD efficiencies for the IDR scaffolds were 68% (IDR = 25%), 99.78% (IDR = 50%), and 93.9% (IDR = 75%). Evidently, 25% IDR demonstrated the lowest efficiency, which can be attributed to inadequate surface area for the immobilization of the catalyst. On the other hand, the 75% IDR scaffold exhibited the highest catalyst loading; however, its PCD performance was slightly inferior to that of the 50% IDR. Such disagreement is likely attributed to the increased structural density, which may prevent light penetration. Claes *et al.*[74] similarly reported that in packed bed reactors, whereby fewer structural features increased catalyst density but imposed more light-scattering limits, hence lowering overall efficiency. In the as-fabricated 3DH, the denser infill possibly triggered internal light attenuation, therefore restricting the photocatalyst's efficacy. The 50% IDR scaffold recorded the highest PCD efficiency (99.78%), due to an optimal balance of exposed surface area and catalyst distribution. Thereby being used in the subsequent investigations.

(iii) Initial concentration of p-cresol. The initial concentration of *p*-cresol (C_0) is a crucial parameter for evaluating the PCD potency of a $Bi_4O_5I_2$@3DH, particularly under constant irradiation time (4 h). In this regard, the activity of $Bi_4O_5I_2$@3DH was assessed across a range of C_0 values (1–50 mg L^{-1}), as shown in Fig. 3e. The results revealed a progressive decline in PCD efficiency with increasing C_0. Specifically, for concentrations up to

Published on 18 November 2025. Downloaded by Guangxi University on 1/30/2026 3:08:27 AM.

20 mg L^{-1}, nearly complete PCD (~100%) was achieved within 4 h reactions, identifying 20 mg L^{-1} as the threshold for the comprehensive pollutant breakdown under the given conditions. The subsequent decline in PCD (beyond 20 mg L^{-1}) can be ascribed to the limited availability of active sites on $Bi_4O_5I_2$@3DH,[75] which were insufficient to degrade higher pollutant concentrations.[4,26] Hence, the C_0 of 20 mg L^{-1} was used in the subsequent analysis.

(iv) Initial pH of aqueous solution. Typically, the pH of the aqueous medium plays a pivotal role in the PCD of pollutants, as it governs both pollutant adsorption and catalyst stability.[4,76] In the current examination, the pH of the *p*-cresol solution was varied from 2.5 to 12.5 to assess its impact on PCD efficiency (Fig. 3f). Reasonably consistent with our previous study,[26] the highest PCD was attained at unadjusted pH 6.5 (99.78%) followed by approximately 10% and 4% decline at pH 7.5 and 5, respectively. However, a marked drop in PCD can be perceived at extreme pH values (2.5 and 12.5), consistent with bismuth oxyiodide materials-based investigations.[4,26]

The zeta potential analysis revealed a point of zero charge (PZC) of 5.5 for the hematite/$Bi_4O_5I_2$ composite, indicating a positively charged surface below this pH and a negative charge above it.[26] Meanwhile, the dissociation constant (pK_a) of *p*-cresol (~10.3)[77,78] dictates its speciation: the neutral form dominates below pH 10.3, transitioning to its anionic form beyond this value (Fig. S5a). Thus, the decline in PCD efficiency at pH > 10.3 can be attributed to electrostatic repulsion between the negatively charged catalyst surface and anionic *p*-cresol, which hinders adsorption. Additionally, excess OH^- ions may scavenge photogenerated hydroxyl radicals (˙OH), as reported by Malefane[79] and Xiong *et al.*,[80] thereby reducing the availability of reactive species. Moreover, the redox potential of ˙OH radicals decreases under alkaline conditions, contributing to the diminished photocatalytic activity at mild alkalinity.[81,82] Therefore, pH 6.5 is optimal for PCD using $Bi_4O_5I_2$@3DH, with a recommended operational range between pH 5 and 10.

3.4. DFT-supported charge transfer mechanism in $Bi_4O_5I_2$@3DH heterojunction

Experimental results confirmed the formation of an *S-scheme* heterojunction between hematite and $Bi_4O_5I_2$,[26] but several properties at the interface are still challenging to determine using only analytical techniques. These include the precise nature of charge redistribution at the heterointerface, local variations in band alignment, and the influence of intrinsic defects on electronic behavior. Such factors are crucial for understanding the charge transfer path and establishing the internal electric field (IEF). Therefore, DFT simulations were carried out to gain atomistic insight into the structural and electronic interactions within the $Bi_4O_5I_2$@3DH composite that underpin its photocatalytic performance.

3.4.1. DFT simulation of the interaction between hematite and $Bi_4O_5I_2$. After geometry optimization, the lattice parameters obtained for the bulk structures were: $a = b = 5.17$ Å, $c = 13.86$ Å, $\alpha = \beta = 90.0°$, $\gamma = 120.0°$ for hematite; and $a = 10.93$ Å, $b = 5.64$ Å, $c = 14.63$ Å, $\alpha = 90.00°$, $\beta = 98.26°$, $\gamma = 90.0°$ for $Bi_4O_5I_2$.

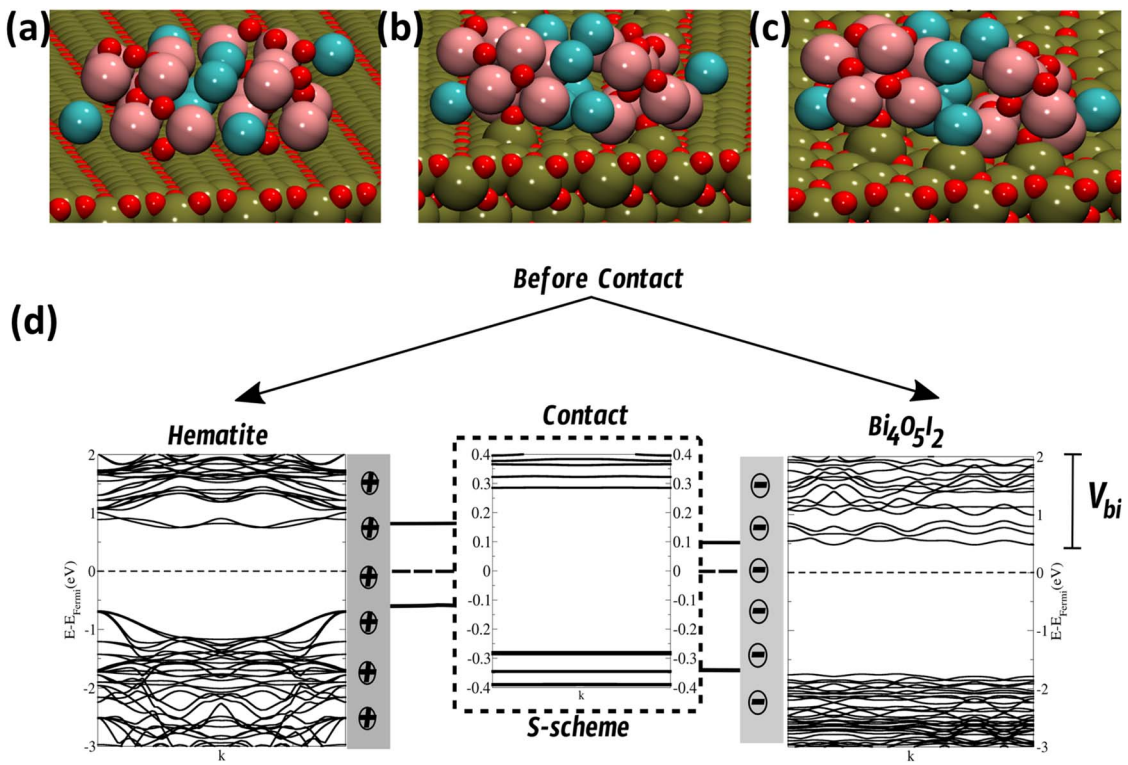

Fig. 4 Deposition of $Bi_4O_5I_2$ on hematite (001): (a) initial configuration with the flake positioned above the substrate; (b) intermediate state during optimization; (c) final structure showing interfacial Fe–O. (d) Band structure evolution of the $Bi_4O_5I_2$/hematite heterojunction.

 This journal is © The Royal Society of Chemistry 2026

Published on 18 November 2025. Downloaded by Guangxi University on 1/30/2026 3:08:27 AM.

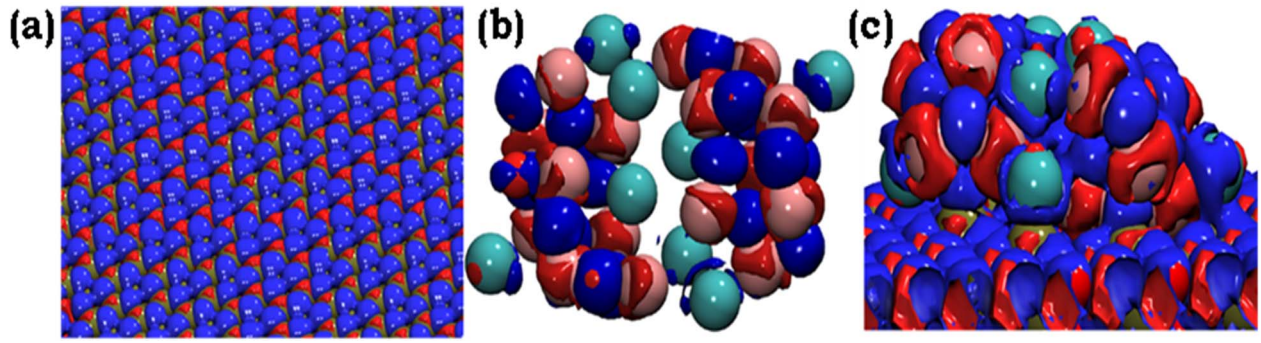

Fig. 5 Charge density difference ($\Delta\rho$) maps. (a) Top view of the hematite (001) monolayer; (b) isolated $Bi_4O_5I_2$ flake; (c) side view of the hematite/$Bi_4O_5I_2$ heterostructure interface. Red and blue isosurfaces represent regions of electron depletion ($\Delta\rho < 0$) and accumulation ($\Delta\rho > 0$), respectively, highlighting the interfacial charge transfer.

These values are in good agreement with the experimental data, with deviations of approximately 3%,[26] confirming the accuracy of the computational method employed. Regarding the surfaces used for constructing the heterostructure, we selected those with higher structural stability and without significant deformation, based on insights from the literature as well as X-ray diffraction (XRD) results. For the hematite (001) surface, the optimized $4 \times 4 \times 1$ supercell presents the following parameters: $a = b = 21.04$ Å, $c = 56.68$ Å, $\alpha = \beta = 90.0°$, $\gamma = 120.0°$.

Regarding their electronic properties, the values calculated for hematite and $Bi_4O_5I_2$ in their respective bulk forms are consistent with experimental data and recent literature, exhibiting deviations of less than 10%.[26,83,84] For the hematite (001) monolayer used to model the substrate, comparisons with theoretical and experimental data must consider the strong dependence of the electronic band gap on the slab thickness. For systems with dimensions similar to those employed in the present study, the simulations reported in the literature show a comparable trend in band gap values.[85] Finally, for the heterojunction, our results reproduce the same trend observed experimentally, with the simulations indicating a reduction of approximately 67% in the electronic band gap. It is worth noting that such discrepancies are expected when using the *Perdew–Burke–Ernzerhof (PBE)* functional,[6] which is known to underestimate band gap values.[86]

Based on the agreement between the calculated structural and electronic properties[26] and the available experimental data, we proceeded to model the deposition process of $Bi_4O_5I_2$ onto the hematite substrate. Fig. 4a shows the initial configuration of the system, with the hematite (001) substrate, periodic along the x and y directions, and the $Bi_4O_5I_2$ flake positioned at an initial height of approximately 3.5 Å. During the structural optimization, $Bi_4O_5I_2$ moves closer to the substrate, resulting in a vertical displacement of some Fe atoms within the hematite structure (Fig. 4b). When considering an isolated $Bi_4O_5I_2$ fragment, some atoms lack full valence coordination and tend to form bonds with atoms from the substrate. In the final optimized geometry, shown in Fig. 4c, the formation of Fe–O bonds at the interface is observed. Importantly, Fig. 4c shows a displacement of an Fe atom close to an I atom, but no bond formations were found.

In the context of investigating photolysis and PCD of cresols (*p*-cresol, *o*-cresol, and *m*-cresol), employing 3DH and $Bi_4O_5I_2$, as well as their surface-based combinations, we aimed to elucidate the electronic phenomena occurring at the semiconductor interface. These interfacial effects are directly linked to the efficiency observed in the photocatalytic processes, as discussed in the experimental section. In this regard, Fig. 4d illustrates the evolution of the electronic band structure of the heterostructure formed between hematite and $Bi_4O_5I_2$, highlighting two key stages: the isolated electronic structures and the interface formed upon contact. We see in Fig. 4d the structures of the two isolated semiconductors $Bi_4O_5I_2$ and hematite, both of which exhibit behavior typical of n-type semiconductors, with their Fermi levels located closer to the conduction band. Understanding this initial alignment is essential for elucidating the nature of the heterojunction formed. The electronic structure no longer reflects a classic p–n junction but instead indicates the formation of a heterojunction of the *S-scheme* type, as shown by the band bending and spatial charge redistribution at the interface. In the *S-scheme* model, photogenerated electrons in the conduction band of $Bi_4O_5I_2$ and holes in the valence band of hematite are preserved after recombination of the less energetic carriers across the interface. The resulting band alignment, with a narrowed interfacial band gap (~0.6 eV), enables efficient separation of charge carriers, crucial for enhanced photocatalytic performance.

The realignment of Fermi levels upon contact leads to a built-in potential (V_{bi}), facilitating the migration of charge carriers and forming a depletion region characterized by the *S-scheme* interface. As illustrated in Fig. 4d, the shaded areas and charge symbols indicate the recombination of lower-energy carriers while preserving the more reactive ones on opposite sides of the junction.

We also investigated the influence of point defects (vacancies) in both materials. In general, the semiconducting character of the materials is preserved in the presence of oxygen or iodine vacancies, which are thermodynamically more likely to occur. However, the removal of a Fe atom from hematite introduces metallic states, resulting in a more significant perturbation of the crystal lattice. Nevertheless, such a defect is

Published on 18 November 2025. Downloaded by Guangxi University on 1/30/2026 3:08:27 AM.

considered less probable in this type of nanomaterial. Additionally, we observed that the presence of vacancies can reduce the work function by up to 1.5 eV, reaching values near 2.5 eV. Although the reduction affects the interfacial potential barrier, it does not inhibit the formation of the *S-scheme* heterojunction. Our findings suggest that vacancy-free models provide a more accurate representation of the experimentally observed behavior. Finally, we analyzed the charge transfer process between the hematite substrate and the $Bi_4O_5I_2$ flake based on the charge density variation illustrated in Fig. 5. The variation provides a spatial representation of how the electrons are redistributed throughout the system. In the context of heterostructures, the charge density difference ($\Delta\rho$) is particularly significant, as it reveals the interfacial charge transfer between the system's components. Regions with $\Delta\rho > 0$, represented in blue, indicate electron accumulation and, thus, an increase in negative charge. In contrast, regions with $\Delta\rho < 0$, shown in red, reflect electron depletion and a reduction in negative charge.

In the (001) hematite monolayer, shown in Fig. 5a, $\Delta\rho$ is negative around the Fe atoms and positive around the O atoms, which is consistent with the structural features of the monolayer. Upon removal of periodicity along the direction now occupied by the vacuum, some oxygen atoms are left with incomplete valence shells, facilitating a degree of electron donation from neighboring Fe atoms while maintaining the material's structural integrity. In Fig. 5b, a predominant electron gain is observed on the oxygen atoms, which is expected since oxygen requires relatively few electrons to complete its valence shell, leading the structure to seek a new electronically stable configuration. At the interface, illustrated in Fig. 5c, the analysis focuses on regions where Fe–O bonds are formed. A net charge loss is observed on the Fe atoms, accompanied by a corresponding charge gain on atoms belonging to the $Bi_4O_5I_2$ flake. To quantify the observed charge transfer, we calculated the difference in the total charge of each atom composing the (001) hematite monolayer before and after contact with $Bi_4O_5I_2$. The results reveal a net charge loss of approximately −0.9 electrons from the hematite side. Applying the same method to $Bi_4O_5I_2$, we obtained a net gain of +0.9 electrons after contact with the hematite substrate. Despite charge transfer, the total net charge of the (001) monolayer/$Bi_4O_5I_2$ system remained overall neutral, and the net transfer of approximately −0.9 electrons from hematite to $Bi_4O_5I_2$ supports the classification of both materials as n-type semiconductors, with hematite acting as the electron donor and $Bi_4O_5I_2$ as the electron acceptor. The resulting redistribution and recombination of charge carriers at the interface confirm the formation of an *S-scheme* heterojunction, with an internal electric field (IEF) oriented from hematite to $Bi_4O_5I_2$. This configuration provides an ideal environment for charge separation and enhanced photocatalytic activity, particularly in cresol degradation reactions.

Importantly, the DFT+U results, including band alignment, charge transfer analysis from hematite to $Bi_4O_5I_2$, and semiconducting characteristics, are consistent with the formation of an *S-scheme* heterojunction. and aligned well with our previous study.[26] Accordingly, a schematic representation of the validated *S-scheme* mechanism is provided in Fig. 6a, illustrating the induction of an IEF directed from hematite (RP: reduction photocatalyst) to $Bi_4O_5I_2$ (OP: oxidation photocatalyst).[87,88] However, charge carriers are photoexcited and spatially separated within their respective semiconductors upon light irradiation. The photogenerated holes in the valence band of OP participate in the oxidation of water molecules to produce hydroxyl radicals (˙OH), while the electrons in the conduction band of RP reduce oxygen molecules to form

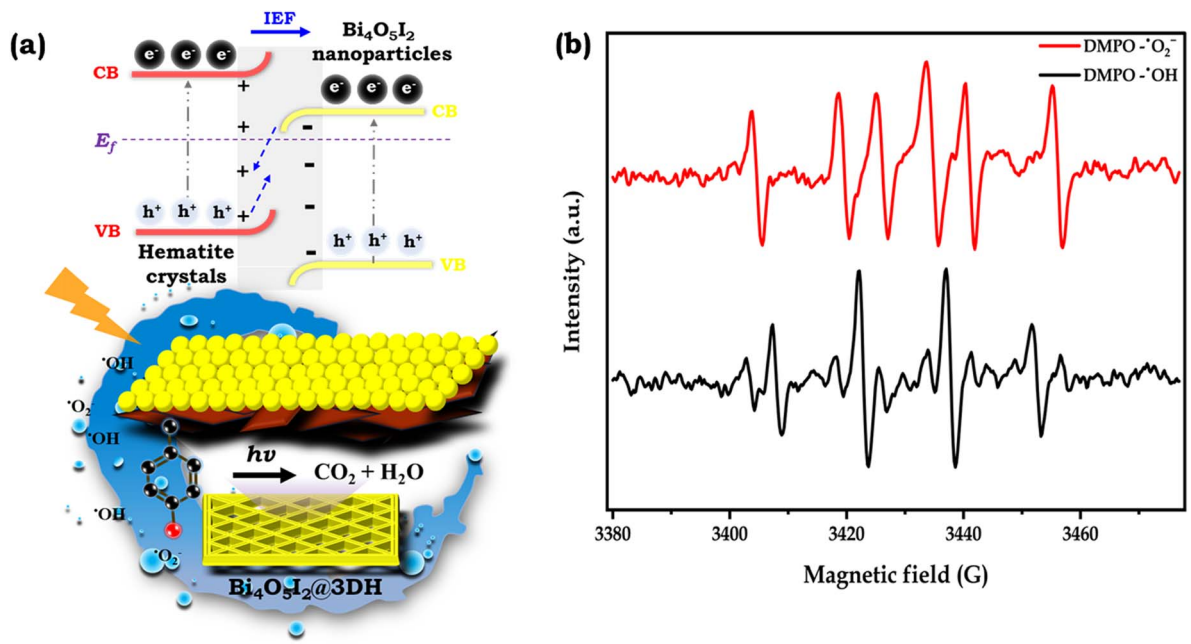

Fig. 6 (a) Electrons and holes transfer mechanism at the heterointerface of hematite and $Bi_4O_5I_2$ photocatalysts. (b) Electron paramagnetic resonance spectra of DMPO-˙O_2^- and DMPO-˙OH adduct signals after 20 min irradiation.

 This journal is © The Royal Society of Chemistry 2026

Published on 18 November 2025. Downloaded by Guangxi University on 1/30/2026 3:08:27 AM.

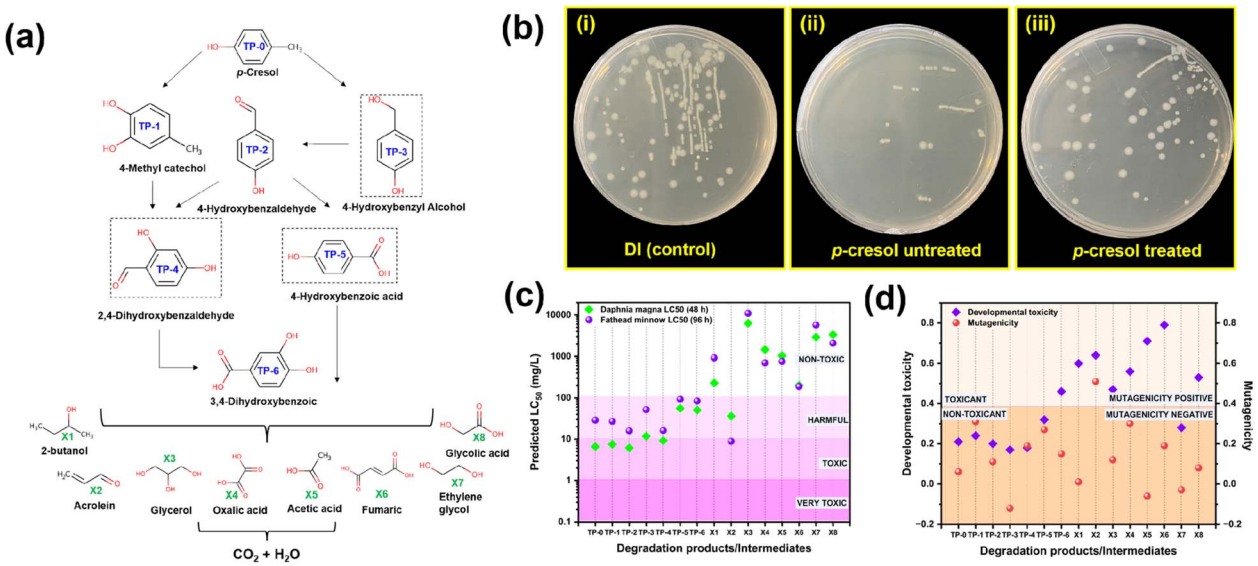

Fig. 7 (a) Plausible degradation pathways of *p*-cresol. (b) *In vitro* (CFU) bio-toxicity test: (i) DI water, *i.e.*, control, (ii) untreated *p*-cresol sample, and (iii) 240 min photocatalytically degraded *p*-cresol sample. QSAR model-based TEST software profiles: (c)* predicted LC_{50} values for *Daphnia magna* (48 h) and *Fathead minnow* (96 h), and (d)† binary endpoints, *i.e.*, developmental toxicity and mutagenicity. [*Very toxic (≤1 mg L^{-1}), toxic (2–10 mg L^{-1}), harmful (11–100 mg L^{-1}), and non-toxic (≥100 mg L^{-1}).[91] †If calculated score < 0.5, then activity = negative else if calculated score ≥ 0.5, then activity = positive[91]].

superoxide radicals ($^{\bullet}O_2^-$). These reactive oxygen species (ROS) then work synergistically to degrade cresols into intermediates, eventually mineralizing them into CO_2 and H_2O. Meanwhile, low-energy charge carriers recombine at the heterointerface,[89] enhancing the selectivity and efficiency of the PCD process. In addition, electron paramagnetic resonance (EPR) spectroscopy was employed to confirm the generation of these radicals. As shown in Fig. 6b, the characteristic DMPO-$^{\bullet}O_2^-$ and DMPO-$^{\bullet}OH$ adduct signals were detected after 20 min of visible light irradiation, thereby validating the radical formation during photocatalysis.[26]

3.5. *In vitro* and *in silico* bio-toxicity assessment

As evident from Fig. S6, the 4 h light irradiation on $Bi_4O_5I_2$@3DH composite led to the partial mineralization of aqueous *p*-cresol (TOC removal efficiency, *i.e.*, TRE 74.63%), resulting in the formation of various intermediate and degradation products (IDPs). In order to identify these IDPs, four representative samples were extracted from the photocatalytic reactor at t = −30, 60, 120, and 240 min. Subsequently, the extracted samples were analyzed using LC-MS/MS, and the IDPs were identified based on their m/z ratios in the mass spectra shown in Fig. S7, which were further corroborated by literature reports.[89,90] Accordingly, the plausible degradation pathways of *p*-cresol were illustrated in Fig. 7a, showing the transformation of the parent compounds into various IDPs denoted as TP-n (where n = 0, 1, 2…), followed by their eventual mineralization into CO_2 and H_2O, as explained in Section S6 of SI.

In the *in vitro* test, explicit CFU disparity was observed among the three Petri dishes (Fig. 7b); the DI water (control) exhibited the highest CFUs, followed by a photocatalytically treated sample and lastly, the untreated sample, shown in Fig. 7b(i–iii). These observations demonstrate the reduction in bio-toxicity after PCD, and the resemblance of CFUs between control and treated samples advocates the reduced bio-toxicity induced by the IDPs.

On the other hand, to conduct the *in silico* ecotoxicity assessment, a QSAR model-based TEST software[55] was used, which estimated crucial ecotoxicological endpoints based on molecular structure. These endpoints include acute aquatic toxicity (*e.g.*, LC_{50} for *Daphnia magna* and *fathead minnow*), binary endpoints (mutagenicity and developmental toxicity, referred to as DT), and bioaccumulation factor (BCF). The predicted results for the IDPs of *p*-cresol are summarized in Table S2, which includes their chemical structures, LC_{50} values, and corresponding ecotoxicological profiles. Based on their LC_{50} values, the *p*-cresol is categorized as "harmful" according to the Globally Harmonized System of Classification and Labelling of Chemicals (GHS).[91] However, *p*-cresol showed negative DT, suggesting no significant DT. These findings are detailed in Table S2. Furthermore, the IDPs displayed varied toxicity profiles, with LC_{50} and binary endpoints delineated in Fig. 7c and d, respectively. Consistent with the CFU observations, the toxicity parameters predicted using TEST also indicated a reduction in the ecotoxicity associated with the various IDPs.

3.6. Practical significance of $Bi_4O_5I_2$@3DH composite

3.6.1. Application of $Bi_4O_5I_2$@3DH in various water matrices. To enable commercial applications, a catalyst must be strong enough to withstand the complex and often unfavorable conditions of various real water matrices, such as tap water, pond water, and secondary treatment effluent (STE) from a sewage treatment plant (STP). Table S3 of the SI provides the physico-chemical characteristics of these matrices. The PCD of *p*-cresol using $Bi_4O_5I_2$@3DH was evaluated under the optimized operational conditions described in Section 3.3.1. As shown in

Published on 18 November 2025. Downloaded by Guangxi University on 1/30/2026 3:08:27 AM.

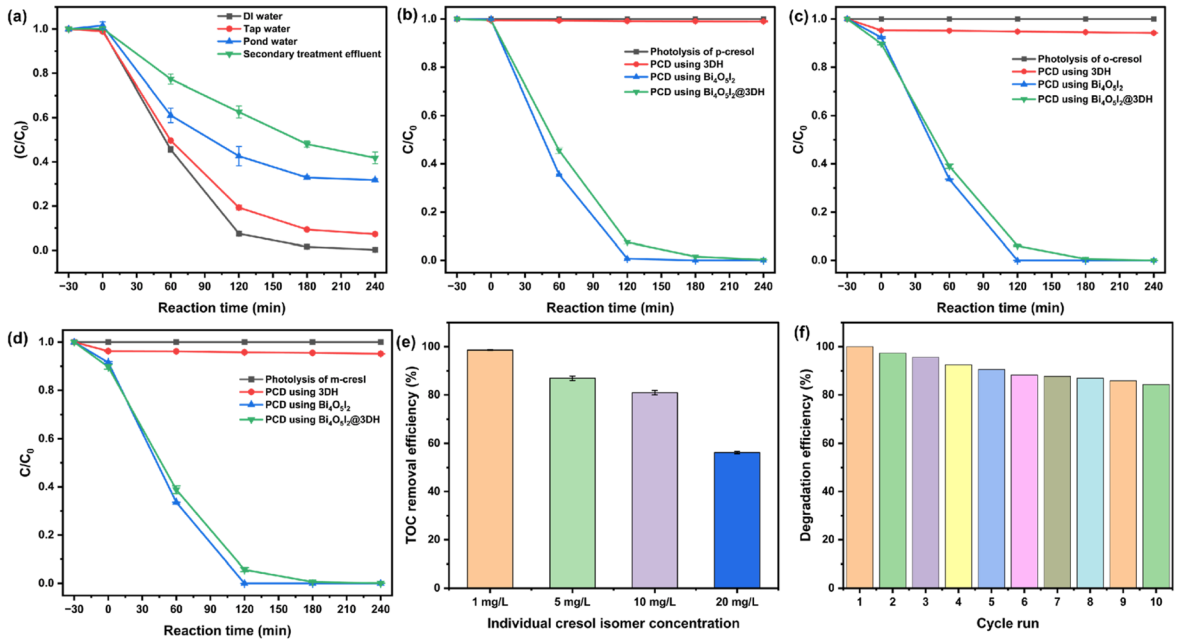

Fig. 8 Practical significance of Bi4O5I2@3DH composite: (a) application of $Bi_4O_5I_2$@3DH in various water matrices, the individual PCD performance of (b) *p*-cresol, (c) *o*-cresol and (d) *m*-cresol. (e) Simultaneous degradation of the isomeric mixture was evaluated in terms of TOC removal efficiency and (f) reusability of as-fabricated $Bi_4O_5I_2$@3DH scaffold over 10 cycles.

Fig. 8a, the highest PCD was achieved in tap water (92.72%), followed by pond water (68.26%) and STE (58.21%). Compared to the control (DI water), the reduced photocatalytic activity in real water matrices is attributed to the presence of co-existing ions and organic/inorganic constituents, which interfere with the degradation process through radical scavenging (*e.g.*, by anions), light attenuation (due to turbidity and chemical oxygen demand, COD), and deactivation of active sites (by COD and nitrate).[92] The observed trend in PCD efficiency (tap water > pond water > STE) is consistent with previous photocatalytic studies on real water matrices and corresponds to the increasing levels of interfering substances reported in Table S3, with the highest in STE and the lowest in tap water.[4,26,93] These findings highlight the applicability of the $Bi_4O_5I_2$@3DH composite across diverse water matrices.

3.6.2. Simultaneous removal of cresols. In addition to co-existing ions, co-existing organic contaminants represent another critical challenge that catalysts encounter in the PCD process's real-world applications. In this regard, the PCD of a mixture of cresol isomers (*p*-cresol, *m*-cresol, and *o*-cresol) was examined under the optimized conditions using the $Bi_4O_5I_2$@3DH scaffold. The initial concentrations of each isomer in the mixture varied from 1 mg L^{-1} to 20 mg L^{-1}. Moreover, the individual PCD performance of *p*-cresol, *m*-cresol, and *o*-cresol is presented in Fig. 8b–d.

Of note, owing to the similar retention times of *p*-, *o*-, and *m*-cresol (provided in Section S4), the overlapping HPLC peaks were observed in samples containing the cresol mixture. Such overlap could lead to an inaccurate assessment of individual degradation efficiencies. Therefore, the simultaneous degradation of the isomeric mixture was evaluated in terms of TRE, as shown in Fig. 8e. The TRE decreased from 98.74% to 56.17% as the initial concentration of the cresol isomers increased from 1 mg L^{-1} to 20 mg L^{-1}, indicating a concentration-dependent reduction in PCD efficiency. However, at 20 mg L^{-1}, the TREs for the individual isomers (Fig. S6) were 74.63% (*p*-cresol), 72.51% (*o*-cresol), and 71.88% (*m*-cresol), suggesting that the presence of multiple isomers significantly affected the overall photocatalytic performance of $Bi_4O_5I_2$@3DH.

3.6.3. Reusability and stability test. Although immobilization facilitates catalyst recovery from aqueous systems, its long-term stability and reusability must also be carefully evaluated to ensure sustained performance in practical applications. In this context, the $Bi_4O_5I_2$@3DH structure was subjected to ten consecutive PCD cycles of *p*-cresol under optimized conditions. As shown in Fig. 8f, only a decrease of 15.72% in degradation efficiency was observed, which may be attributed to the gradual loss of photocatalyst and active sites during reuse.[94] However, the inductively coupled plasma mass spectrometry (ICP-MS) analysis confirmed that any leaching of active components was below the instrument's detection limit, indicating good chemical stability. Importantly, the photocatalyst was reused in successive cycles without any further cleaning or regeneration. The synthesized $Bi_4O_5I_2$@3DH exhibited good structural stability and reusability, underlining its potential for use in continuous-flow reactors for real-field applications.

In addition, Table S4 presents a contrasting overview of the PCD performance of $Bi_4O_5I_2$@3DH scaffold and other reported immobilized photocatalyst systems targeting PCs. Notably, the present study distinguishes itself by achieving near-complete degradation of cresol isomers under visible-light irradiation using a 50 W LED source.

 This journal is © The Royal Society of Chemistry 2026

Published on 18 November 2025. Downloaded by Guangxi University on 1/30/2026 3:08:27 AM.

4. Conclusions

The present study demonstrates the development of a $Bi_4O_5I_2$-decorated 3D-printed hematite scaffold ($Bi_4O_5I_2$@3DH) for the efficient PCD of cresol isomers under visible light. Unlike conventional inert supports (*e.g.*, glass or ceramic), the engineered photoactive hematite scaffold synergistically contributes to the photocatalytic activity *via* interfacial charge transfer with $Bi_4O_5I_2$, as confirmed by DFT+U simulations. Moreover, the DIW-based 3D printing approach allowed precise control over infill density, which provided a high exposed surface area, facilitating enhanced photon–catalyst interactions. Consequently, the optimized $Bi_4O_5I_2$@3DH achieved nearly complete *p*-cresol degradation (99.78%) with minimal adsorption, indicating superior efficiency across diverse water matrices and in the presence of multiple cresol isomers. Remarkably, the current photocatalyst system exhibited high reusability, structural robustness, and partial mineralization with reduced ecotoxicity. Thus, establishes its potential as a scalable, sustainable, and field-deployable system for water and wastewater remediation.

Author contributions

Akash Rawat: conceptualization, methodology, experiments, data analysis, validation, visualization, writing – original draft. Raphael Benjamim de Oliveira: conceptualization of the system components interaction, methodology, simulations, data analysis. Tapas Pal: experiments, data analysis, writing – original draft. Kleuton Antunes: conceptualization of the system components interaction, methodology, simulations, data analysis. Raphael Tromer: conceptualization of the *S-scheme* junction, methodology, simulations, data analysis. Marcelo Lopes Pereira Junior: idealization of structures, theoretical analysis, writing – original draft. Guilherme S. L. Fabris: theoretical analysis and writing – original draft. Adarsh Singh: experiments, data analysis, writing – original draft. Ashok Kumar Gupta: supervision, resources, review, and editing. Douglas Soares Galvão: supervision, resources, review, editing. Chandra Sekhar Tiwary: supervision, resources, review, editing.

Conflicts of interest

There are no conflicts to declare.

Data availability

p-cresol (including their corresponding toxicity profiles), the physico-chemical characteristics of the real water matrices, and the parameters used in DIW for the hematite grid printing are provided in the

The data related to the intermediate and degradation products (IDPs) of *p*-cresol (including their corresponding toxicity profiles), the physico-chemical characteristics of the real water matrices, and the parameters used in DIW for the hematite grid printing are provided in the supplementary information (SI). Additional datasets supporting the remaining findings of this study are available from the corresponding author upon reasonable request. Supplementary information is available. See DOI: https://doi.org/10.1039/d5ta07867a.

Acknowledgements

Akash Rawat, Tapas Pal, and Adarsh Singh are thankful to the Indian Institute of Technology Kharagpur, India, for financial support. Guilherme S. L. Fabris thanks the postdoc scholarship financed by the São Paulo Research Foundation (FAPESP) (process number 2024/03413-9), and R. B. O. thanks "National Council for Scientific and Technological Development" (CNPq) process numbers 151043/2024-8 and 200257/2025-0. R. M. T. acknowledges financial support from CNPq (grant 307371/2025-5). M. L. P. J. acknowledges financial support from FAPDF (grant 00193-00001807/2023-16), CNPq (grant 444921/2024-9), and CAPES (grant 88887.005164/2024-00). Douglas S. Galvão acknowledges the Center for Computing in Engineering and Sciences at Unicamp for financial support through the FAPESP/CEPID Grant (process number 2013/08293-7). We thank the Coaraci Supercomputer for computer time (process number 2019/17874-0) and the Center for Computing in Engineering and Sciences at Unicamp (process number 2013/08293-4). C. S. T. acknowledges DAE Young Scientist Research Award (DAEYSRA), and AOARD (Asian Office of Aerospace Research and Development) grant no. FA2386-21-1-4014. C. S. T. acknowledges DST-AMT, SPARC and Naval Research Board. A. K. G. and C. S. T. acknowledges Central Public Health and Environmental Engineering Organisation CPHEEO, MoHUA.

References

1 A. K. Gupta and S. Ayoob, *Fluoride in Drinking Water*, CRC Press, 2016.
2 A. Rawat, A. Srivastava, A. Bhatnagar and A. K. Gupta, *J. Cleaner Prod.*, 2023, **383**, 135382.
3 A. Singh, A. Srivastava, D. Saidulu and A. K. Gupta, *J. Environ. Manage.*, 2022, **317**, 115305.
4 A. Rawat, S. K. Srivastava, C. S. Tiwary and A. K. Gupta, *J. Environ. Chem. Eng.*, 2024, **12**, 112879.
5 I. M. S. Pillai and A. K. Gupta, *J. Electroanal. Chem.*, 2015, **756**, 108–117.
6 N. Mate, K. Nabeela, G. Preethikumar, S. Pillai and S. M. Mobin, *Mater. Horiz.*, 2024, **11**, 5114–5122.
7 C. Kennes, R. Mendez and J. M. Lema, *Water Res.*, 1997, **31**, 1549–1554.
8 D. Arya, S. Kumar and S. Kumar, *J. Hazard. Mater.*, 2011, **198**, 49–56.
9 National Institute of Medical (NIM) DrugBank, *Cresols Profile*, https://pubchem.ncbi.nlm.nih.gov/compound/Cresol#section=Solubility, accessed 6 December 2024.
10 S. Kumar, D. Arya, A. Malhotra, S. Kumar and B. Kumar, *J. Environ. Chem. Eng.*, 2013, **1**, 865–874.
11 L. Zou, Y. Wang, C. Huang, B. Li, J. Lyu, S. Wang, H. Lu and J. Li, *Sci. Total Environ.*, 2021, **754**, 142219.
12 S. Bera, H. Kauser and K. Mohanty, *J. Water Process Eng.*, 2019, **31**, 100842.

Published on 18 November 2025. Downloaded by Guangxi University on 1/30/2026 3:08:27 AM.

13 S. K. Kuila, D. K. Gorai, B. Gupta, A. K. Gupta, C. S. Tiwary and T. K. Kundu, *Chemosphere*, 2021, **268**, 128780.
14 N. Panigrahy, M. Barik, R. K. Sahoo and N. K. Sahoo, *Int. Biodeterior. Biodegrad.*, 2020, **147**, 104837.
15 USEPA, *Code of Federal Regulations*, https://www.ecfr.gov/current/title-40/chapter-I/subchapter-D/part-116#116.4, accessed 6 December 2024.
16 K. V. A. Kumar, L. Chandana, P. Ghosal and C. Subrahmanyam, *Mol. Catal.*, 2018, **451**, 87–95.
17 E. P. Melián, O. G. Díaz, J. Araña, J. M. D. Rodríguez, E. T. Rendón and J. A. H. Melián, *Catal. Today*, 2007, **129**, 256–262.
18 Y. Zhu and P. Kolar, *J. Environ. Chem. Eng.*, 2014, **2**, 2050–2058.
19 K.-R. Lee and C.-S. Tan, *Ind. Eng. Chem. Res.*, 2000, **39**, 1035–1038.
20 Y. Zhang, L. Zhuang, B. Ji, Y. Ren, X. Xu, J. He, Y. Xue and H. Sun, *J. Environ. Manage.*, 2025, **375**, 124208.
21 M. Mahdavianpour, G. Moussavi and M. Farrokhi, *Process Biochem.*, 2018, **69**, 153–160.
22 Y. Feng, H. Li, L. Ling, S. Yan, D. Pan, H. Ge, H. Li and Z. Bian, *Environ. Sci. Technol.*, 2018, **52**, 7842–7848.
23 J. Lim, H. Kim, J. Park, G.-H. Moon, J. J. M. Vequizo, A. Yamakata, J. Lee and W. Choi, *Environ. Sci. Technol.*, 2020, **54**, 497–506.
24 C. Wang, J. Tian, Q. Tan, J. Xie, G. Chen, Y. Chen and X. Mao, *Environ. Sci. Technol.*, 2025, **59**, 9865–9885.
25 F. Dong, Z. Wang, Y. Li, W.-K. Ho and S. C. Lee, *Environ. Sci. Technol.*, 2014, **48**, 10345–10353.
26 A. Rawat, S. K. Srivastava, C. S. Tiwary and A. K. Gupta, *J. Mater. Chem. A*, 2025, **13**, 1271–1286.
27 D. E. Willis, E. C. Sheets, M. R. Worbington, M. Kamat, S. K. Glass, M. J. Caso, T. Ofoegbuna, L. M. Diaz, C. Osei-Appau, S. D. Snow and K. M. McPeak, *ACS ES&T Eng.*, 2023, **3**, 1694–1705.
28 V. K. Parida, S. K. Srivastava, S. Chowdhury and A. K. Gupta, *Langmuir*, 2023, **39**, 18846–18865.
29 D. Saidulu, A. Bhatnagar and A. Kumar Gupta, *Sep. Purif. Technol.*, 2024, **350**, 128002.
30 G.-B. Fu, R. Xie, J.-W. Qin, X.-B. Deng, X.-J. Ju, W. Wang, Z. Liu and L.-Y. Chu, *Ind. Eng. Chem. Res.*, 2021, **60**, 8762–8775.
31 D.-H. Lim, H. Ali Maitlo, S. A. Younis and K.-H. Kim, *Mater. Today Nano*, 2024, **27**, 100499.
32 P. Lisowski, J. C. Colmenares, O. Mašek, W. Lisowski, D. Lisovytskiy, A. Kamińska and D. Łomot, *ACS Sustainable Chem. Eng.*, 2019, **7**, 16933–16934.
33 J. Liu, T. Du, P. Chen, Q. Yue, H. Wang, L. Zhou and Y. Wang, *Appl. Surf. Sci.*, 2024, **664**, 160274.
34 S. K. Loeb, P. J. J. Alvarez, J. A. Brame, E. L. Cates, W. Choi, J. Crittenden, D. D. Dionysiou, Q. Li, G. Li-Puma, X. Quan, D. L. Sedlak, T. David Waite, P. Westerhoff and J.-H. Kim, *Environ. Sci. Technol.*, 2019, **53**, 2937–2947.
35 S. Guo, X. Gao, Y. Huang, R. Zhou, F. Chen, C. Cai, K. Zhou and R. Chen, *ACS ES&T Water*, 2025, **5**, 33–41.
36 P. Ghosal, B. Gupta, R. S. Ambekar, M. M. Rahman, P. M. Ajayan, N. Aich, A. K. Gupta and C. S. Tiwary, *Adv. Sustainable Syst.*, 2022, **6**(3), 2100282.
37 R. S. Ambekar, A. Joseph, S. Ganji, R. Agrawal, G. Nirmal and C. S. Tiwary, *Ceram. Int.*, 2024, **50**, 44447–44456.
38 S. Ng, M. Sanna, E. Redondo and M. Pumera, *J. Mater. Chem. A*, 2024, **12**, 396–404.
39 S. Roy Barman, P. Gavit, S. Chowdhury, K. Chatterjee and A. Nain, *JACS Au*, 2023, **3**, 2930–2947.
40 R. Das, R. B. de Oliveira, B. Kumar, V. Mishra, S. Sarkar, S. Sarkar, I. d. M. Felix, L. D. Machado and C. S. Tiwary, *Adv. Eng. Mater.*, 2025, **27**(2), 2401747.
41 M. A. S. R. Saadi, A. Maguire, N. T. Pottackal, M. S. H. Thakur, M. M. Ikram, A. J. Hart, P. M. Ajayan and M. M. Rahman, *Adv. Mater.*, 2022, **34**, 2108855.
42 Y. Majooni, S. O. Abioye, K. Fayazbakhsh and N. Yousefi, *ACS ES&T Water*, 2024, **4**, 1952–1965.
43 P. Wei, C. E. Cipriani and E. B. Pentzer, *Matter*, 2021, **4**, 1975–1989.
44 J. Z. Y. Tan, M. A. Ávila-López, A. Jahanbakhsh, X. Lu, J. Bonilla-Cruz, T. E. Lara-Ceniceros, J. M. Andresen and M. M. Maroto-Valer, *J. Mater. Chem. A*, 2023, **11**, 5408–5426.
45 S. Ng, R. Zazpe, J. Rodriguez-Pereira, J. Michalička, J. M. Macak and M. Pumera, *J. Mater. Chem. A*, 2021, **9**, 11405–11414.
46 P. Wei, H. Leng, Q. Chen, R. C. Advincula and E. B. Pentzer, *ACS Appl. Polym. Mater.*, 2019, **1**, 885–892.
47 Q. Chen, P. Cao and R. C. Advincula, *Adv. Funct. Mater.*, 2018, **28**(21), 1800631.
48 R. S. Ambekar, A. Joseph, S. Ganji, G. Nirmal, R. Agrawal and C. S. Tiwary, *Adv. Eng. Mater.*, 2024, **26**(7), 2301830.
49 Z. Yang, L. Li, J. Gao, S. Zeng, J. Cui, S. Shao, K. Wang, D. Ma, C. Hu and Y. Zhao, *ACS ES&T Eng.*, 2022, **2**, 2142–2149.
50 L. Wang, J.-C. Zhou, Z.-H. Li, X. Zhang, K. M. Y. Leung, L. Yuan and G.-P. Sheng, *Environ. Sci. Technol.*, 2023, **57**, 21835–21845.
51 C. Kim, S. Chae, Y. Park and W. Choi, *ACS ES&T Eng.*, 2022, **2**, 232–241.
52 Z. Xiao, J. Xiao, L. Yuan, M. Ai, F. Idrees, Z.-F. Huang, C. Shi, X. Zhang, L. Pan and J.-J. Zou, *J. Mater. Chem. A*, 2024, **12**, 5366–5376.
53 A. T. Rasool, A. Nazir, Q. Zhang and E. Li, *J. Environ. Chem. Eng.*, 2025, **13**, 117750.
54 W. Zhang, Q. Tan, T. Liu, Y. He, G. Chen, K. Chen, D. Han, D. Qin and L. Niu, *Mater. Horiz.*, 2023, **10**, 5869–5880.
55 U.S. Environmental Protection Agency, *Toxicity Estimation Software Tool (TEST)*, version 5.1, U.S. EPA, Washington, DC, 2025.
56 S. S. Nath, I. G. Patil and P. Sundriyal, *J. Energy Storage*, 2024, **79**, 110129.
57 L. Moreno-Sanabria, C. Ramírez, M. I. Osendi, M. Belmonte and P. Miranzo, *Adv. Mater. Technol.*, 2022, **7**(9), 2101455.
58 R. S. Ambekar, A. Joseph, S. Ganji, G. Nirmal, R. Agrawal and C. S. Tiwary, *Adv. Eng. Mater.*, 2024, 2301830.
59 D. Zhang, C. Chu, S. Ma, Y. Wang, C. Duan, J. Guo, X. Shi, G. Xu, Y. Cheng and A. Sun, *J. Alloys Compd.*, 2023, **931**, 167632.

 This journal is © The Royal Society of Chemistry 2026

Published on 18 November 2025. Downloaded by Guangxi University on 1/30/2026 3:08:27 AM.

60 Z. Ye, C. Chu, D. Zhang, S. Ma, J. Guo, Y. Cheng, G. Xu, Z. Li and A. Sun, *Mater. Today Commun.*, 2021, **28**, 102534.
61 J. A. Lewis, J. E. Smay, J. Stuecker and J. Cesarano, *J. Am. Ceram. Soc.*, 2006, **89**, 3599–3609.
62 T. V. Neumann and M. D. Dickey, *Adv. Mater. Technol.*, 2020, **5**(9), 2000070.
63 B. S. Haile, V. Pal, T. Pal, S. Slathia, G. M. Jigi, S. D. Negedu, N. Tiwari, H. Singh, A. Joseph, F. E. Olu and C. S. Tiwary, *Adv. Eng. Mater.*, 2025, **27**(7), 2402283.
64 O. Moradlou, Z. Rabiei, A. Banazadeh, J. Warzywoda and M. Zirak, *Appl. Catal., B*, 2018, **227**, 178–189.
65 R. L. Blake, R. E. Hessevick, T. Zoltai and L. W. Finger, *Am. Mineral.*, 1966, **51**(1–2), 123–129.
66 X. Xiao, C. Xing, G. He, X. Zuo, J. Nan and L. Wang, *Appl. Catal., B*, 2014, **148–149**, 154–163.
67 E. Keller, V. Krämer, M. Schmidt and H. Oppermann, *Z. Kristallogr. - Cryst. Mater.*, 2002, **217**, 256–264.
68 R. L. Blake, R. E. HessevicK, T. Zoltai and L. W. Finger, *Am. Mineral.*, 1966, **51**, 123–129.
69 F. Mashkoor, M. Shoeb, S. Zhu, H. Jeong and C. Jeong, *J. Mater. Chem. A*, 2025, **13**, 22539–22562.
70 Y. Chen, M. Nisar, W. Qin, Z. Xu, M. H. Danish, F. Li, G. Liang, Z. Ge, J. Luo and Z. Zheng, *Adv. Funct. Mater.*, 2025, **35**(25), 2425050.
71 I. khan, Y. Sun, F. Khan, J. Zhang, A. Kareem, M. Naseem, Z. Ali, M. Sultan, U. Arif, X. Ma and Z. Wu, *Sep. Purif. Technol.*, 2025, **359**, 130472.
72 Y. Chen and D. D. Dionysiou, *Appl. Catal., B*, 2006, **69**, 24–33.
73 M. Long, C. Huang, X. Huang, L. Yang, L. Chen, K. Sun, C. Wang, L. Zhang, L. Zhang, S. Cai, S. Yao, H. Zhu, T. Yang, B. Zou and T. Liu, *Mater. Horiz.*, 2024, **11**, 6476–6485.
74 T. Claes, T. Van Gerven and M. E. Leblebici, *Chem. Eng. J.*, 2021, **403**, 126355.
75 B. Gupta, D. Saidulu, A. Srivastava, A. Rawat, A. Singh, A. Bhatnagar and A. K. Gupta, *J. Environ. Chem. Eng.*, 2023, **11**, 110128.
76 R. Li, X. Song, Y. Huang, Y. Fang, M. Jia and W. Ma, *J. Mol. Catal. A: Chem.*, 2016, **421**, 57–65.
77 National Center for Biotechnology Information, *PubChem Compound Summary for CID 2879, P-Cresol*, https://pubchem.ncbi.nlm.nih.gov/compound/P-Cresol.
78 P. J. Pearce and R. J. J. Simkins, *Can. J. Chem.*, 1968, **46**, 241–248.
79 M. E. Malefane, *ACS Omega*, 2020, **5**, 26829–26844.
80 X. Xiong, X. Zhang, S. Liu, J. Zhao and Y. Xu, *Photochem. Photobiol. Sci.*, 2018, **17**, 1018–1022.
81 C. Zhu, Y. Wang, L. Qiu, Y. Liu, H. Li, Y. Yu, J. Li and W. Yang, *Sep. Purif. Technol.*, 2022, **290**, 120878.
82 C. Lai, F. Huang, G. Zeng, D. Huang, L. Qin, M. Cheng, C. Zhang, B. Li, H. Yi, S. Liu, L. Li and L. Chen, *Chemosphere*, 2019, **224**, 910–921.
83 N. Naveas, R. Pulido, C. Marini, J. Hernández-Montelongo and M. M. Silván, *iScience*, 2023, **26**, 106033.
84 R. Yin, Y. Li, K. Zhong, H. Yao, Y. Zhang and K. Lai, *RSC Adv.*, 2019, **9**, 4539–4544.
85 A. C. M. Padilha, M. Soares, E. R. Leite and A. Fazzio, *J. Phys. Chem. C*, 2019, **123**, 16359–16365.
86 M. Jain, J. R. Chelikowsky and S. G. Louie, *Phys. Rev. Lett.*, 2011, **107**, 216806.
87 N. Ojha, K. K. Pant and E. Coy, *Ind. Eng. Chem. Res.*, 2023, **62**, 21885–21908.
88 H. Deng, X. Fei, Y. Yang, J. Fan, J. Yu, B. Cheng and L. Zhang, *Chem. Eng. J.*, 2021, **409**, 127377.
89 H. Yang, R. Wang, H. Hou, Y. Li, Z. Li, H. Wang, X. Zhan, D. Zhang, Z. Liang, Y. Luo and W. Yang, *Sep. Purif. Technol.*, 2025, **362**, 131819.
90 R. Khunphonoi and N. Grisdanurak, *Chem. Eng. J.*, 2016, **296**, 420–427.
91 GHS, *Globally Harmonized System of Classification and Labeling of Chemicals (GHS)*, 2021.
92 Y. You, X. Shi, L. Huang, J. Zhao, W. Ji, L. Li, D. Bu and S. Huang, *Mater. Horiz.*, 2025, **12**, 2965–2976.
93 V. K. Parida, S. K. Srivastava, A. K. Gupta and A. Rawat, *Mater. Express*, 2023, 1–38.
94 K. V. S. Rao, M. Subrahmanyam and P. Boule, *Appl. Catal., B*, 2004, **49**, 239–249.